Eckhaus-like instability of large scale coherent structures in a fully turbulent von Karman flow

E Herbert, P.-P Cortet, François Daviaud, Bérengère Dubrulle

PHYSICS OF FLUIDS **26**, 015103 (2014)

Eckhaus-like instability of large scale coherent structures in a fully turbulent von Kármán flow

E. Herbert,[1,a)] P.-P. Cortet,[2] F. Daviaud,[1] and B. Dubrulle[1]
[1]*SPHYNX, Service de Physique de l'État Condensé, DSM, CEA Saclay, CNRS URA 2464, 91191 Gif-sur-Yvette, France*
[2]*Laboratoire FAST, Université Paris-Sud, CNRS, 91405 Orsay Cedex, France*

(Received 21 November 2013; accepted 9 December 2013; published online 9 January 2014)

The notion of instability of a turbulent flow is introduced in the case of a von Kármán flow thanks to the monitoring of the spatio-temporal spectrum of the velocity fluctuations, combined with projection onto suitable Beltrami modes. It is shown that the large scale coherent fluctuations of the flow obey a sequence of Eckhaus instabilities when the Reynolds number Re is varied from 10^2 to 10^6. This sequence results in modulations of increasing azimuthal wavenumber. The basic state is the laminar or time-averaged flow at an arbitrary Re, which is axi-symmetric, i.e., with a 0 azimuthal wavenumber. Increasing Re leads to non-axisymmetric modulations with increasing azimuthal wavenumber from 1 to 3. These modulations are found to rotate in the azimuthal direction. However, no clear rotation frequency can be established until $\mathrm{Re} \approx 4 \times 10^3$. Above, they become periodic with an increasing frequency. We finally show that these modulations are connected with the coherent structures of the mixing shear layer. The implication of these findings for the turbulence parametrization is discussed. Especially, they may explain why simple eddy viscosity models are able to capture complex turbulent flow dynamics.
[http://dx.doi.org/10.1063/1.4855018]

I. INTRODUCTION

In classical phenomenology, turbulence arises after a sequence of symmetry breakings, successive instabilities, or bifurcations, which however progressively restore the system symmetries in a statistical sense.[1] The study of these instabilities traditionally proceeds from (linear or nonlinear) perturbations of the so-called "basic state," the stationary laminar solution of the Navier-Stokes (NS) equation at low Reynolds number. At finite Reynolds number there is no general well-defined criterion to discriminate between the turbulent or laminar nature of the flow: one cannot define clearly a critical threshold beyond which the flow is turbulent and below which it is laminar. The consensus view is that the flow is turbulent when the Reynolds number is large enough and when a well established spatio-temporal energy spectrum is observed with broadband power laws. In such a case, a possible statistical equivalent of the laminar "basic state" can be defined using the (statistically or time) averaged flow. This flow is stationary by construction, but differs from a usual basic state in the sense that it is solution of the ensemble averaged Navier-Stokes equation instead of a solution of the plain Navier-Stokes equation. A natural question then arises: what happens once the statistically stationary turbulent state is reached? Is this the end of the story or can new instabilities of the averaged turbulent flow develop? Experimentally, the answer seems to be positive, since spontaneous bifurcations and flow reversals in fully developed turbulence have already been observed: (i) in a wake flow, there is a mean pattern transition at a critical Reynolds number. This corresponds to the so-called "drag-crisis" (see Ref. 2). This leads to a dramatic decrease of the mean drag of a sphere or a cylinder in a turbulent flow for a critical value of the Reynolds number

a)eric.herbert@univ-paris-diderot.fr

Re $\sim 10^5$. The wake becomes narrower as the mean flow pattern changes. (ii) Spontaneous flow reversals have been observed in thermally driven (Rayleigh-Bénard) convection, both experimentally[3] and numerically.[4,5] In a cylindrical Rayleigh-Bénard geometry, the reversals of large scale circulation were reported to be induced by reorientation along the azimuthal direction.[6] However, it is difficult to experimentally characterize a bifurcation from a non-stationary or periodic flow. (iii) In a magnetohydrodynamic turbulence, the large scale magnetic field spontaneously generated in a liquid metal at Re $> 10^6$ was shown[7] to undergo spontaneous reversals, with a dynamics governed by a few magnetic modes despite the strongly turbulent background. This observation led to a simple model of geodynamos with a few modes undergoing chaotic dynamics.[8] An open problem common to all these situations is to find suitable tools to study and characterize these types of instabilities.

The purpose of this paper is to present some answers to these questions in the specific case of a von Kármán flow. This flow is generated by two counter-rotating impellers in a cylindrical vessel. At low Reynolds number, the laminar flow is axi-symmetric and divided into two toric recirculation cells separated by an azimuthal shear layer. Its transition to turbulence for various counter-rotations and aspect ratio has been extensively studied theoretically, numerically, and experimentally with smooth or rough (fitted with blades) impellers (see, e.g., Refs. 9–16 and references therein). The study in Ref. 13 was performed in the exact-counter-rotating case. It was reported that a first bifurcation from the stationary and axi-symmetric laminar state occurs at Re $= 175$, yielding a stationary flow with an azimuthal modulation, i.e., for which the axisymmetry is broken. This stationary state persists up to typically Re ~ 300 where time-dependence arises. The transition to turbulence further proceeds through plain, modulated, or chaotic traveling waves, until Re $\sim 10^4$, where a "fully developed turbulent state" seems to have been reached. In that state, the energy spectrum is broad and the dimensionless dissipation does not depend on Reynolds number anymore.[13] In that turbulent state, the flow once time averaged regains the structure of the basic laminar flow, made of two shearing toric recirculation cells. In the present paper, we have worked using the same experimental setup. We demonstrate that the flow is organized into large scale coherent structures. These structures are subject to a sequence of Eckhaus type instabilities leading to an increasing azimuthal wavenumber as the Reynolds number varies from 10^2 to 10^6, similar to the sequence of instabilities at much lower Re. Since this sequence of instabilities occurs on coherent structures in a turbulent flow rather than a laminar "basic state," we are facing a new paradigm that both require new tools of investigations and open interesting questions about turbulence parametrization. The tools are presented in Sec. II, the instability is described in Sec. III and some theoretical consequences are discussed in Sec. IV.

II. TECHNICAL BACKGROUND AND TOOLS

A. Experimental setup

We have worked with a von Kármán flow generated by two coaxial and counter-rotating impellers in a cylindrical vessel. More details about the experimental setup can be found in Ref. 17. The cylinder radius and height are $R = 100$ mm and $H = 180$ mm, respectively. The impellers consist of 185 mm diameter disks fitted with 16 curved blades of 20 mm height. The impellers are driven by two independent motors. The motor frequencies are, respectively, set to f_1 and f_2. In the present work, the impellers are rotating with the convex face of the blades going forwards, contrarily to Ref. 13. The working fluid is either pure water, a water-glycerol mixture (26%–74% in weight, respectively), or pure glycerol. The resulting accessible Reynolds numbers, $\mathrm{Re} = \pi(f_1 + f_2)R^2\nu^{-1}$ with ν the kinematic viscosity, vary from 10^2 to 10^6.

This setup is invariant under $\mathcal{R}_\pi$ rotations around any radial axis passing through the center of the cylinder. Measurements are done thanks to a Stereoscopic Particle Image Velocimetry (S-PIV) system. The S-PIV provides time series of the 3 components of the velocity (radial $v_x(x, z, t)$, vertical $v_z(x, z, t)$, and azimuthal $v_y(x, z, t)$) on a 63×58 points grid in a meridian plane $[x, z]$ composed of two planes dephased by π in the cylindrical coordinates. $x = r\cos(\varphi_0)$, with the azimuthal angle $\varphi_0 = [0, \pi]$ and r the radial distance from the impellers axis. z is the vertical distance from the center of the cylinder, y is the out-of-plane direction, and t is the time. The azimuthal component is then written in the cylindrical coordinates using $v_\varphi(x, z, t) = x/|x|\, v_y(x, z, t)$. The size of the recorded

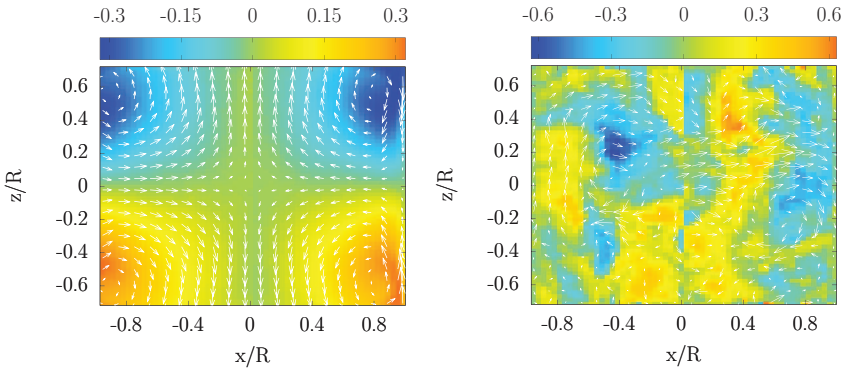

FIG. 1. Left, time-averaged velocity field $\bar{\mathbf{v}}$, measured in a meridian plane using S-PIV, at $\mathrm{Re} = 10^6$ and $\theta = (f_1 - f_2)/(f_1 + f_2) = 0$. $x = r\cos\varphi_0$, $\varphi_0 = [0, \pi]$. Right, corresponding instantaneous fluctuating component of the velocity field $\mathbf{v}' = \mathbf{v} - \bar{\mathbf{v}}$. The color maps the azimuthal velocity v_φ (normalized by $R(f_1 + f_2)/2$) whereas the arrows map the (v_x, v_z) velocities.

images is $194.9 \times 144.3\ \mathrm{mm}^2 = 58\,\delta_R \times 63\,\delta_Z$ (where $\delta_R = 3.3$ mm and $\delta_Z = 2.3$ mm are the spatial resolutions of the S-PIV). Time series have sampling frequency in the range $f_s = 1.7$ to 15 Hz and are composed of $N = 1200$ to 4200 samples. Each experiment is started with the impellers and the fluid at rest. The impeller velocities are then suddenly increased to reach their target values. After a few tens of seconds, a statistically stationary state is reached and S-PIV time series is finally acquired.

B. Experimental perturbation analysis

For low Reynolds number $\mathrm{Re} \leq 500$, the flow is steady and laminar and only few fluctuations are present. When $\theta = (f_1 - f_2)/(f_1 + f_2) = 0$, the instantaneous flow is composed of two toric recirculation cells separated by an azimuthal shear layer located at $z = 0$ reflecting the R_π-symmetry of the system. Increasing the Reynolds number, one expects to reach fully developed turbulence around $\mathrm{Re} = 10^4$ as observed in Ref. 13, with increasing difference between the instantaneous flow and the time-averaged flow. Above $\mathrm{Re} = 500$ and at $\theta = 0$, the axisymmetry is broken by fluctuations of the instantaneous flow. However, this symmetry is restored for the time-averaged flow (cf. Fig. 1), at any Reynolds number. By construction, this average flow is time-independent and will be the equivalent of a "basic state." As the Reynolds number is increased, this "basic state" is subject to increasingly stronger fluctuations.[18] The question we want to address here is: are these fluctuations purely disorganized as in thermal noise or can we identify a pattern in them when varying the Reynolds number,[19] in a way similar to a sequence of bifurcations of ordinary instabilities? To answer this question we need two steps: (i) to separate the fluctuations into "organized" motions and "thermal" noise and (ii) to build a suitable tool to study the temporal behavior of these organized motions. These steps are described below. For step (i), we use comparison with and projection onto Beltrami modes. For step (ii), we use spatio-temporal spectra, as used in wave turbulence.[20]

1. Projection onto Beltrami modes

The measured velocity fields time series are analyzed thanks to a projection on the basis of Beltrami modes as detailed in Ref. 21. Beltrami modes have been introduced as a general spectral decomposition basis,[22] and any velocity field in a cylindrical geometry can be decomposed as a superposition of such modes. Given a vector field, $\mathbf{v}$, lying in a cylinder of radius $R = 1$ and height $H = 2h$, with usual cylindrical components $\mathbf{v} = (v_r, v_\varphi, v_z)$, we first switch to the new components $\mathbf{V} = (V_+, V_-, v_z)$ such that $V_\pm = (v_r \pm i\, v_\varphi)/2$. The field $\mathbf{V}$ can further be decomposed over Beltrami modes $\mathbf{B}^{\mathbf{nmks}}$ as

$$\mathbf{V} = \sum_{n=1}^{N} \sum_{m=-M}^{M} \sum_{k=-Pk_0}^{Pk_0} \sum_{s=(-)}^{(+)} D_{nmk} \mathbf{B}^{\mathbf{nmks}}, \tag{1}$$

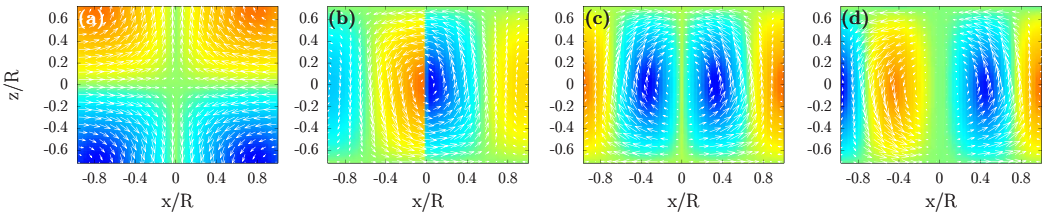

FIG. 2. (a) (resp., (b), (c), and (d)) synthetic velocity field $\mathbf{b^{nmk}}$ obtained from corresponding Beltrami modes $\mathbf{B^{nmk}}$ in a meridional plane with $n = k/k_0 = 1$ and $m = 0$ (resp., $m = 1$, 2, and 3). Same color and arrow codes as in Fig. 1.

where $k_0 = \pi/h$, n and m are integer numbers, and (N, M, P) are the number of considered modes in the (r, φ, z) directions, respectively. The D_{nmk} are complex amplitudes which conjugates verify $D^*_{nmk} = D_{n,-m,-k}$ and the Beltrami modes are given by

$$\mathbf{B^{nmks}} = \begin{pmatrix} B_+^{nmks} \\ B_-^{nmks} \\ B_z^{nmk} \end{pmatrix} = \frac{1}{2} \begin{pmatrix} (\lambda^s - k)\, J_{m+1}(\mu_{nm} r) \\ (\lambda^s + k)\, J_{m-1}(\mu_{nm} r) \\ -2i\,\mu_{nm}\, J_m(\mu_{nm} r) \end{pmatrix} \exp(im\varphi + ikz). \tag{2}$$

Here, $\lambda^s = s\sqrt{\mu_{nm}^2 + k^2}$ with $s = \pm$ and J_m is the Bessel function of order m. The orthogonality condition is ensured by the fact the μ_{nm} coefficients are the nth root of J_m. Equation (1) then corresponds to a decomposition into solenoidal Beltrami waves with polarization given by the sign s of λ^s. From now on, we will omit the s superscript for simplicity. We define the synthetic velocity field $\mathbf{b^{nmk}} = (b_r, b_\varphi, b_z)$ corresponding to $\mathbf{B^{nmk}} = (B_+, B_-, B_z)$ using the real parts of, respectively, $b_r = B_- + B_+$, $b_\varphi = i(B_- - B_+)$, and $b_z = B_z$ and a fixed sign of λ. Some examples of the synthetic velocity fields obtained for $k/k_0 = n = 1$ and $m = 0$, 1, 2, 3 in the two planes $\varphi_0 = [0, \pi]$ are provided in Fig. 2. The recirculation cells, the shear layer, and the axi-symmetry of the experimental time-averaged flow shown in Fig. 1 are well recovered by the φ-invariant $m = 0$ mode shown in Fig. 2(a). We use the boundary condition explained in Ref. 21. When $m > 0$ the velocity fields depend on the azimuthal angle φ and the axi-symmetry is lost. However, for each meridian plane at a fixed $[\varphi_i, \varphi_i + \pi]$ the velocity field shows mirror (anti-)symmetry with respect to the $r = 0$-axis. Even-numbered m velocity fields are found to be symmetric while odd-numbered are found to be anti-symmetric. Introducing the space average $\langle\,\rangle = \int_0^1 r\,dr \int_{-\pi}^{\pi} d\varphi \int_{-h}^{h} dz$ and using the classical properties of the Bessel functions, the orthogonality of $\mathbf{B^{nmk}}$ writes

$$\begin{aligned} \left\langle \mathbf{B^{nmk}} \cdot \mathbf{B^{n'm'k'}*} \right\rangle &= \left\langle B_+^{nmk} B_+^{n'm'k'*} + B_-^{nmk} B_-^{n'm'k'*} + B_z^{nmk} B_z^{n'm'k'*} \right\rangle, \\ &= \left\langle \mathbf{B^{nmk}} \cdot \mathbf{B^{nmk}*} \right\rangle \delta_{mm'} \delta_{nn'} \delta_{kk'}. \end{aligned} \tag{3}$$

This means that for any field satisfying the decomposition (1), we have

$$\left\langle \mathbf{V} \cdot \mathbf{B^{nmk}*} \right\rangle = D_{nmk} \left\langle \mathbf{B^{nmk}} \cdot \mathbf{B^{nmk}*} \right\rangle, \tag{4}$$

which provides a simple way to find the projection of the vector $\mathbf{V}$ on $\mathbf{B^{nmk}}$ by spatial average over the fluid volume. In the experiment, we however have access to velocity measurements in one plane only, corresponding to $\varphi = 0$ and $\varphi = \pi$. This precludes the exact instantaneous projection onto given Beltrami modes. We remedy to these problems by two methods: (i) conditional time averages at a given phase $m\varphi$. This is explained in Sec. III E. (ii) Direct comparison with "synthetic measurements." This is described in Sec. III B.

These projections, limited to low order Beltrami modes, allow to reconstruct synthetic velocity field time series in the full 3D space, accounting for the full spatiotemporal evolution of the "organized" motions of the turbulent flow.

2. Spatio temporal spectrum

In traditional instability analysis, it is customary to draw space-time diagrams to detect wavelike pattern, see Refs. 23 and 24. In a turbulent system with a wide range of scales, a natural generalization is to resort to spatio-temporal spectra. This approach is routinely used in the field of wave turbulence (see Ref. 25 for a recent review) and led to computation of dispersion relations, see Ref. 20. To obtain these spectra from our experimental PIV measurements, we proceed as follows. From time series of the azimuthal velocity $v_\varphi(x, z, t)$ in the meridian plane we compute the time-averaged velocity field $\bar{v}_\varphi$ and its fluctuations $v'_\varphi(x, z, t)$ defined by $v'_\varphi = v_\varphi - \bar{v}_\varphi$. From the corresponding time series, the full space-time (2D in space and 1D in time) power spectrum $E(k_x, k_z, f)$ is computed, where $k = K/2\pi$ with K the wavevector and $f = \omega/2\pi$ is the frequency. This is done in two steps. First, the instantaneous spatial (2D) Fourier Transform $\tilde{v}'_{2D}(k_x, k_z, t)$ for each time t of the time series is computed. Then, the temporal Fourier Transform of $\tilde{v}'_{2D}$ using a window size composed of n time steps is computed. Finally, $\tilde{v}'_{3D}(k_x, k_z, f)$ is obtained that leads to the spatio-temporal power spectrum in 3 dimensions $E(k_x, k_z, f)$:

$$E(k_x, k_z, f) = |\tilde{v}'_{3D}|^2 = \left| \int dx\, dz\, dt v'_\varphi(x, z, t)\, e^{i(\omega t + k_x x + k_z z)} \right|^2 . \tag{5}$$

Spatial (horizontal and vertical) and temporal resolutions of the spectra are comprised in the ranges $(1/(2R), 1/(2\delta_R))$, $(1/H, 1/(2\delta_Z))$, and $(f_s/n, f_s/2)$, respectively.

3. Synthetic time series

Direct comparison of the experimental spectra with synthetic ones, based on a synthetic velocity fields time series, is then performed. The latter were obtained with single Beltrami modes of a given (cylindrical) geometry. For simplicity, we have restricted our comparison with modes with large-scale poloidal structure $n = k/k_0 = 1$ and varying azimuthal structure (variable m). As soon as $m > 0$, the axisymmetry is broken. Like in any rotation-breaking instability, it is natural to expect that the corresponding perturbation mode will rotate with a frequency f_r (that is *a priori* small with respect to the impellers rotation rate $(f_1 + f_2)/2$). The corresponding Beltrami modes will then have the structure:

$$\mathbf{B}^{1mk_0} \sim \exp(im\varphi + ikz - if_r t). \tag{6}$$

An artificial time series of such a mode is build in the meridional plane $[x, z]$. These synthetic data are then processed like the experimental signal to get synthetic space-time power spectra. Since the perturbation Beltrami mode is periodic (with m the number of period) in its azimuthal direction, a peak of energy is located at a frequency $f = mf_r$ as can be seen in Fig. 5(h). This peak is well resolved by setting the sampling frequency to a much higher value, typically $50 \times mf_r$. In the sequel, we will refer to the spectra obtained using the experimental (resp., synthetic) data by E_E (resp., E_S).

III. RESULTS

A. Isotropy: Evidence for the Eckhaus instability

A first characterization of the flow perturbation independently of its dynamics can be found by considering the spatial spectrum $E(k_x, k_z)$, obtained through the integration of the 3D spectrum $E(k_x, k_z, f)$ over all temporal frequencies. An example for an experimental flow at $\mathrm{Re} \approx 10^6$ is provided in Fig. 3. The energy is mainly concentrated along the x-axis at $k_z \approx 0$ inside an ellipsoidal region, pointing out the anisotropic structure of the flow. For useful interpretation, we have compared this isotropy measurements with synthetic data. In Fig. 3, we also show an example obtained with $n = k/k_0 = 1$, $m = 3$, and $f_r = 0.2$ Hz synthetic velocity fields time-series. For this field, the overall shape of the spatial spectrum is close to the experimental one. Both spatial spectrum $E_E(k_x, k_z)$ and $E_S(k_x, k_z)$ in Fig. 3 display 2 distinct maxima. They are found around $k_z = 0$ for two values of k_x symmetric with respect to $k_x = 0$. As we can see in Fig. 2 using the synthetic velocity fields or in Fig. 9 using the projection of the experimental fields onto the Beltrami modes, the x-axis traces the

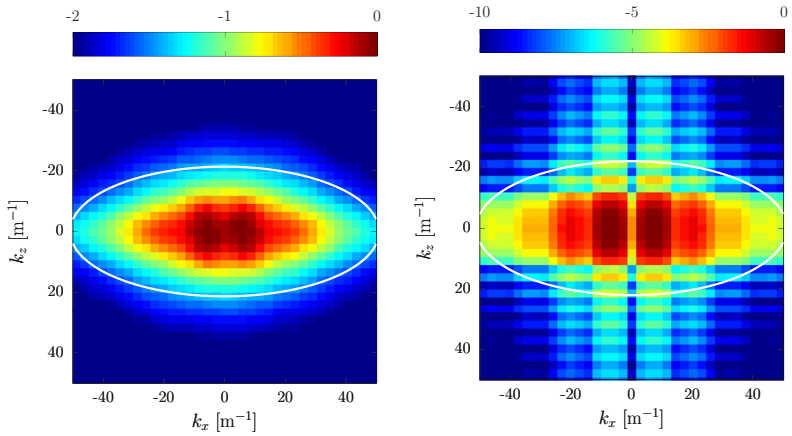

FIG. 3. Left, experimental spatial power spectrum $E_E(k_x, k_z)$ at $\theta = 0$ and Re $\approx 10^6$, from time series from which the flow shown Fig. 1(b) is extracted. White line is an ellipsoidal fit of a fixed energy level contour line. $w/h = 2.5$, with w the width and h the height of the ellipse. Right, synthetic spatial power spectrum $E_S(k_x, k_z)$ with $n = k/k_0 = 1$ and $m = 3$, corresponding to the flow shown Fig. 2(d) rotating at $f_r = 0.2$ Hz and for which $w/h = 2.3$. Colors are log scaled.

parity of m. This parity is reproduced through the spectral analysis in this way: in the even-numbered (resp., odd-numbered) case, the symmetry (resp., anti-symmetry) of the flow with respect to $r = 0$ leads to a fundamental wavelength of roughly the size (resp., half of the size) of the vessel. The wavenumbers $k_x \simeq \pm 1/(2R)$ corresponding to the maxima of energy in the symmetric case approach the resolution limit of the Fourier transform and practically appear as $k_x \simeq 0$ (see Figs. 5(e) and 5(g)). On the contrary, the anti-symmetric case leads to two distinguishable symmetric peaks at $k_x \approx \pm 1/R$ (see Figs. 5(f) and 5(h)). Experimentally, these different patterns are reproduced using the Reynolds number as a driving parameter. Figures 5(a) and 5(c) at Re = 714 and 7200 show the symmetric (even) case whereas Figs. 5(b) and 5(d) at Re = 1473 and 10^6 show the anti-symmetric (odd) case. Consequently, the flow is experiencing successive transitions in parity. To study more precisely the evolution of this pattern with the Reynolds number, one can concentrate on the 1D-spatial spectrum $E_E(k_x)$, obtained through integration of $E_E(k_x, k_z)$ over all k_z. This was done for all values of Re resulting in Fig. 4. One observes clear transitions at Re = 700, 3200, and 8800, where

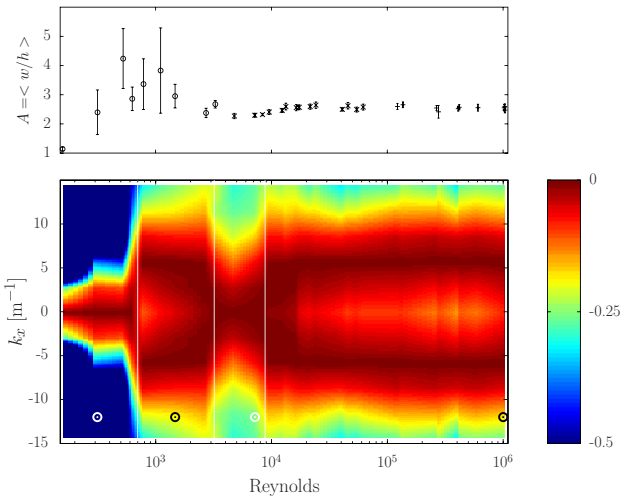

FIG. 4. Top, anisotropy factor $A = \langle w/h \rangle$ computed from experimental power spectra as a function of the Reynolds number (see details in the text and illustration in Fig. 3). Marker shapes ($\circ$, $\times$, $+$) represent the different working fluids. Bottom, experimental $E_E(k_x)$ at $\theta = 0$ as a function of the Reynolds number. Each spectrum is normalized by its maximum. Colors are log scaled. Vertical white lines mark strong transitions in the $E_E(k_x)$ spectrum which highlight parity changes in the structure of the experimental flow. Black and white circles, see Fig. 5.

the maximum of the 1D-spatial spectrum shifts back and forth between $k_x = 0$ and two symmetric values $k_x = \pm 7\ \mathrm{m}^{-1}$. Therefore, the kind of transitions observed in Fig. 4 is suggestive of successive azimuthal changes in parity (even-odd-even-odd). This means that the flow is composed of a large scale coherent structure which is experiencing an Eckhaus type instability in its azimuthal direction starting from the axi-symmetric time-averaged flow which is a $m = 0$ mode.

To bring some clues to the upper modes where $m > 0$ we resort to a different analysis of the spatial spectrum. The contour line at a fixed iso-energy level was fitted using a centered ellipsoidal curve, $(x/w)^2 + (z/h)^2 = 1$, with the width w and the height h as fitting parameters. As a result w/h is a measure of the anisotropy of the flow. In order to obtain error bars, the ratio w/h was computed for various iso-energy levels corresponding to different fractions of the total energy of the spectra, from 65 to 90% (resp., 75% to 99%) for E_E (resp., for E_S). The mean value $A = \langle w/h \rangle$ and the standard deviation are finally computed to evaluate both the anisotropy and the error. Using the synthetic data, varying m leads to different values of A which is moreover found not to depend on f_r. Specifically, $A = 2.3 \pm 0.3$, for $m = 0$. For $m = 1$, $A = 5.2 \pm 2.4$ reach its maximum. Increasing m, A tends to decrease, yielding for $m = 2$, 3, and 4 to $A = 2.9 \pm 0.8$, 2.4 ± 0.3, and 2.3 ± 0.3, respectively. We have then studied the experimental evolution of the anisotropy ratio with the Reynolds number. This is shown in Fig. 4. One sees the error bar can be large in particular below $Re = 5000$. Consequently, this approach is not precise enough to determine at which Reynolds number the transitions occurred. However, we clearly distinguish different regimes. The anisotropy starts from a value of about 1.1 at very low Reynolds number where the amplitude of the fluctuations reach the resolution limit of our PIV. Increasing the Reynolds number, A increases up to 2.7 ± 0.7 corresponding to the laminar axi-symmetric ($m = 0$) case where $A = 2.3$ or to the time-averaged flow at any Reynolds number. The amplitude of the anisotropy then reaches a maximum (4.2 ± 1) at $\mathrm{Re} = 800$. This last value is compatible with the odd-numbered $m = 1$ mode. At approximately $\mathrm{Re} = 5000$, A reaches a minimum at 2.3 ± 0.1. Which seems not compatible with even-numbered $m = 2$ mode but could be a $m = 4$ mode. Finally, for Reynolds number larger than 10^4, A shows a plateau around $A = 2.5$, which value is compatible with the odd-numbered $m = 3$ mode.

B. Temporal behaviour

A symmetry breaking generally coincides with a propagative instability.[26] To check this hypothesis and try to measure the rotating frequency f_v of the azimuthal structure of the turbulent flow, we used the 2D-spatio-temporal spectrum $E_E(k_x, f)$ which is computed through the integration over k_z of the 3D-spectrum $E(k_x, k_z, f)$. $E_E(k_x, f)$ is then compared to the spectrum $E_S(k_x, f)$ obtained using a synthetic Beltrami flow for different values of m. This is done in Fig. 5 using different Reynolds numbers. The rotation frequency f_r of the synthetic flows is adjusted to get the best resemblance with the experimental field which is guessed to rotate at a f_v frequency. At $\mathrm{Re} = 314$, the experimental spectrum is found very close to $E_S(k_x, f)$ with $m = 0$. This result can be extended to the time-averaged flow spectra (not shown) at any Reynolds number since it is similar to the laminar instantaneous flow. Increasing the Reynolds number to $\mathrm{Re} = 1473$ (resp., $\mathrm{Re} = 7200$) in a region where one (resp., two) Eckhaus bifurcation(s) has occurred, we observe a strong similarity with corresponding $E_S(k_x, f)$ with $m = 1$ (resp., $m = 2$) with a small but non-zero rotation frequency $f_r = 0.01$ Hz. For the last two cases, the rotation frequency f_v of the azimuthal structure of the flow shall be non-zero. However, it reveals to be smaller than our spectral resolution, typically 0.01 Hz, and therefore remains unmeasurable. Increasing the Reynolds number the energy is found to remain mainly concentrated at a 0 frequency up to $\mathrm{Re} = 4 \times 10^4$. In the vicinity of this last Re the energy becomes distributed on a wider range of frequencies, up to 1.5 Hz. However, no particular frequency is selected. Increasing further the Reynolds number, peaks at non-zero frequencies come up, as shown for $\mathrm{Re} = 10^6$. These peaks are the signature of a fixed rotation frequency at $f_v = 0.7$ Hz. In this case, the experimental spectrum is regained by $E_S(k_x, f)$ with $m = 3$ and $f_r = 0.2$ Hz. Overall, our results are compatible with a rotating frequency bifurcating from a small but non-zero value around $\mathrm{Re} = 4 \times 10^4$.

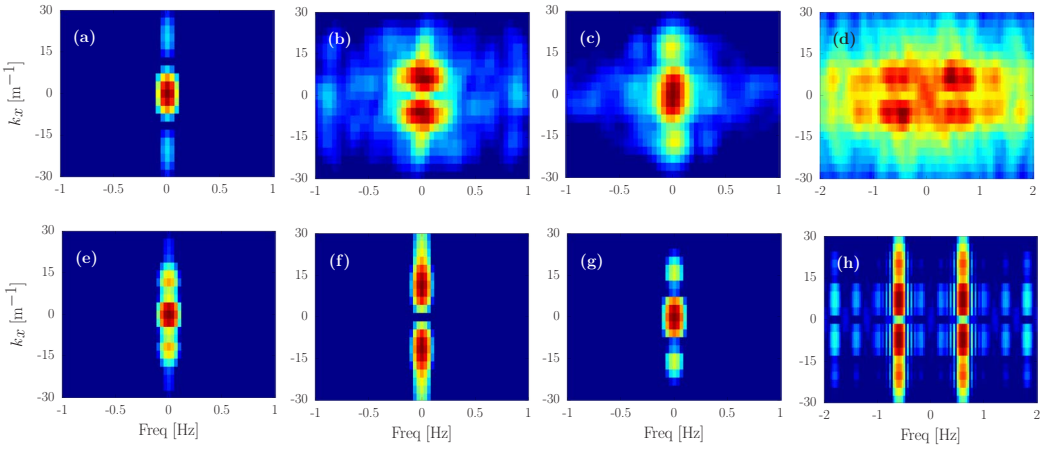

FIG. 5. Top, experimental spatio-temporal spectrum $E_E(k_x, f)$ at $\theta = 0$ for Re $= 314$ (a), 1473 (b), 7200 (c), and 10^6 (d), corresponding to circles in Fig. 4. Colors are log scaled in the range $[-1.5, 0]$. Bottom, synthetic spatio-temporal spectrum $E_S(k_x, f)$, using $n = k/k_0 = 1$ and $f_r = 0.01$ Hz for $m = 0$ (e), 1 (f), 2 (g), and $f_r = 0.2$ Hz for $m = 3$ (h). Colors are log scaled in the range $[-2, 0]$ for ((e)–(g)) and $[-6, 0]$ for (h). Note the frequency axis range change for (d) and (h).

C. Rotation direction

At large enough Reynolds number, we have seen that a $m = 3$ perturbation of the "basic state" of the flow is established with a non-zero rotating frequency. In the perfectly symmetric case there is, however, no general argument imposing the direction of rotation of the pattern. Experimentally, this should be the case at $\theta = 0$. However, our setup was not perfectly symmetric what led to observe the same direction of rotation for all experiments. A slight shift of θ was then introduced to compensate this lack of symmetry. Using this adjustment we observed for each experiment one or the other direction of rotation with an equal probability. The direction of rotation is best seen by focusing on the vertical direction, i.e., looking at the 2D-spatio-temporal spectrum $E_E(k_z, f)$, as shown in Fig. 6. One observes either an upward ($k_z > 0$ when $f > 0$) or a downward ($k_z < 0$ when $f > 0$) tilt of the spatio-temporal spectrum. This can be modelled by considering a synthetic Beltrami spectrum corresponding to $m = 3$ with two opposite rotation directions, leading to an upward or downward tilt of the spectrum (also shown Fig. 6).

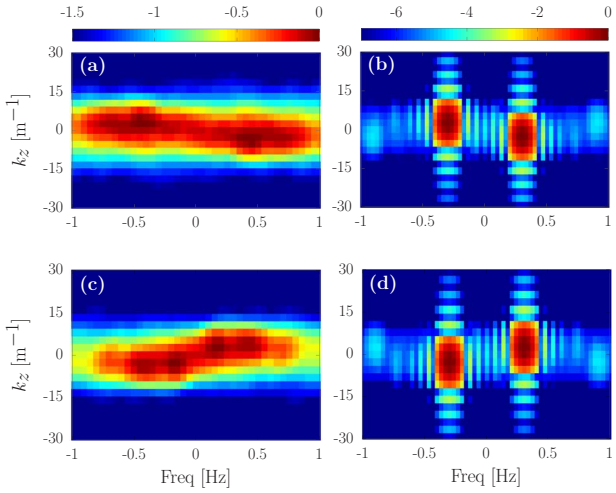

FIG. 6. Left, experimental spatio-temporal spectrum $E_E(k_z, f)$ for (a) $\theta = 0$, Re $\approx 10^6$ and (c) $\theta = -8 \times 10^{-3}$, Re $\approx 8 \times 10^5$. Right, synthetic spatio temporal spectrum $E_S(k_z, f)$ with $n = k/k_0 = 1$, $m = 3$ and using (b) $f_v = 0.1$ Hz and (d) $f_v = -0.1$ Hz. Colors are log scaled.

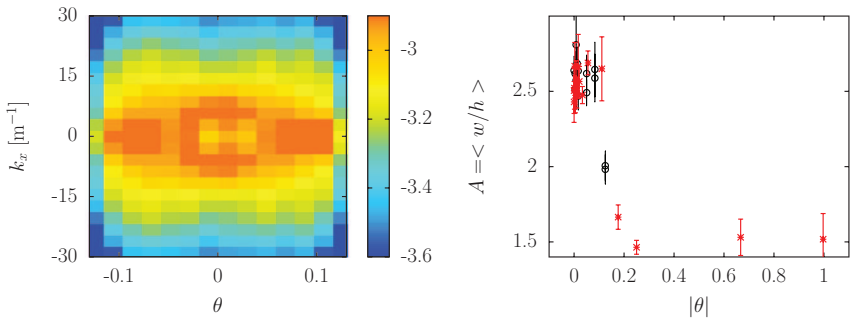

FIG. 7. Left, experimental spatio-temporal spectrum $E_E(k_x, \theta)$ at Re $\approx 10^5$. The shear layer reaches the slower impeller at $\theta = \pm 0.1$. Colors are log scaled. Right, $A = \langle w/h \rangle$ as defined in Fig. 3 as a function of $|\theta|$ at Re $\approx 10^5$ (black circles) and Re $\approx 5 \times 10^5$ (red/gray stars).

D. Link with the shear layer dynamics

It is tempting to associate the Eckhaus azimuthal instability evidenced in Sec. III A to a Kelvin-Helmoltz instability of the shear layer. Indeed, this instability was already pointed out as the physical mechanism for a stability loss of the axi-symmetric steady-state followed by successive flows with non-zero azimuthal wavenumber. This was numerically observed for small Reynolds number (Re < 500) in a geometry[12] close to ours. Here, we report a similar mechanism but at largely higher Reynolds numbers. It was also observed that the Kelvin-Helmoltz instability results in a series of large scale structures taking the shape of radial vortices with well defined azimuthal wavenumber that can be seen, e.g., through bubble seeding and white light.[13,27] The possibility of changes in m of this pattern revealing an Eckhaus instability analog to that existing in small dynamical systems was already mentioned in Ref. 17. To sustain this possibility, we have monitored the 2D-spatial spectrum at a fixed Reynolds number, as a function of θ. It was already reported (see, for example, Ref. 17) a shifting of the shear layer toward the slower impeller with increasing $|\theta|$. When $|\theta| > 0.1$ the shear layer was found to be completely absorbed. If the azimuthal structures we observed are related to the shear layer, the structure of the 2D-spatial spectrum should also follow θ. This is indeed the case, as can be seen in Fig. 7 both from the isotropy and from the 1D-spatial spectrum $E_E(k_x, \theta)$. With increasing $|\theta|$ the two bands of k_x merge into one, at $k_x = 0$. At $|\theta| = 0.1$ the isotropy measurement and the peak at $k_x = 0$ of the spectrum drops suddenly. Further increasing θ, both the isotropy and the spatial spectrum (not shown) are found to be independent of θ. This is indicative of a transition into a $m = 0$ structure, with no azimuthal modulations anymore. This thus proves that the azimuthal modulation is indeed strongly associated with the shear layer.

E. Visualization of the coherent structure

Finally, the existence of organized motions in the turbulent flow means $\mathbf{v}'$ can be written as the sum of an in-phase term and a fluctuation term: $\mathbf{v}' = \mathbf{v_c} + \mathbf{v}''$, with $\mathbf{v}''$ the fluctuations and $\mathbf{v_c}$ the coherent structure velocity field. A visualization of the spatial structure of one azimuthal mode m can then be obtained using conditional average of the velocity field $\mathbf{v}'$. The condition is given by suitable projection onto the corresponding Beltrami mode, see Eq. (4). Due to the geometry of our PIV device, we however only have access to the velocity field in a meridional plane, i.e., for $\varphi_0 = [0, \pi]$. Since the azimuthal modes are rotating we may however replace the azimuthal integration in the scalar product by a suitable time integration. This is made possible for high enough Reynolds number where the rotation frequency of the coherent structure is resolved. We used conditional average as follows: we first compute for each instantaneous experimental field $\mathbf{v}'$ the quantity:

$$a_m(t) = \int_{-1}^{1} x\, dx \int_{-h/R}^{h/R} dz\, \mathbf{v}'(t) \cdot \mathbf{B^{1mk_0}}(x, \varphi_0, z), \tag{7}$$

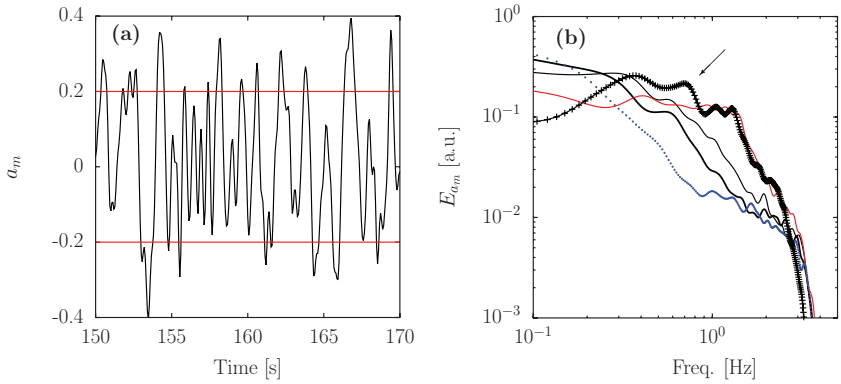

FIG. 8. (a) $a_m(t) = \int x dx \int dz \mathbf{v}' \cdot \mathbf{B^{1mk_0}}$ with $m = 3$ and $\mathrm{Re} = 10^6$ at a fixed angle φ (corresponding to the angle of Fig. 2(c)) as a function of time. $a_m(t)$ was computed using $\mathbf{v}'(t)$ from the time-series used in Fig. 5(d) and was finally low-pass filtered at 4 Hz. Horizontal lines, see Fig. 9. (b) Power spectrum $E_{a_m}(f)$ of $a_m(t)$ (+ solid line) for the data shown in (a) and for other Reynolds numbers: Re/1000 = 41 (thin red/gray line), 21 (thin black line), 12 (thick black line), 7 (○). The arrow marks the main peak evolution with decreasing Re.

keeping the azimuthal wavenumber m and the angle φ constant. A result is shown in Fig. 8(a) obtained using the same experimental data shown in Fig. 5(d) at $\mathrm{Re} = 10^6$ and the synthetic velocity field as in Fig. 2(d) at $m = 3$. One sees quasi-sinusoidal fluctuations in the signal $a_m(t)$. We propose that these fluctuations correspond to the coherent structures passing through the PIV plane. This is corroborated by looking at $E_{a_m}(f)$, the temporal power spectrum of $a_m(t)$ in Fig. 8(b). The rotation frequency measured using the 2D-spectrum of the velocity field and the main peak frequency of E_{a_m} ($f = 0.73$ Hz in this experiment) are found identical. Secondary peak is a sub-harmonic at $f = 0.37$ Hz. For lower Reynolds number, below $\mathrm{Re} = 4 \times 10^4$, both amplitudes of these peaks decrease and are shifted toward lower frequencies. Simultaneously, the energy becomes roughly equally distributed along a plateau, which amplitude is increasing and width is decreasing with the Reynolds number. Down to $\mathrm{Re} = 10^4$ a peak at small amplitude can still be distinguished at $f \approx 0.5$ Hz. For the lower Reynolds number, the plateau vanishes and the energy is mainly concentrated in the vicinity of $f = 0$. This confirms the behavior described in Sec. III B.

The velocity field $\mathbf{v}'$ was then averaged over times for which a_m lies in a given range of values $[a_m > \epsilon]$, representative of a given phase of the velocity field. An example is provided in Fig. 9 for $\epsilon = 0.2$ and $m = 3$ from $a_m(t)$ shown in Fig. 8. One sees the presumable $m = 3$ coherent structure

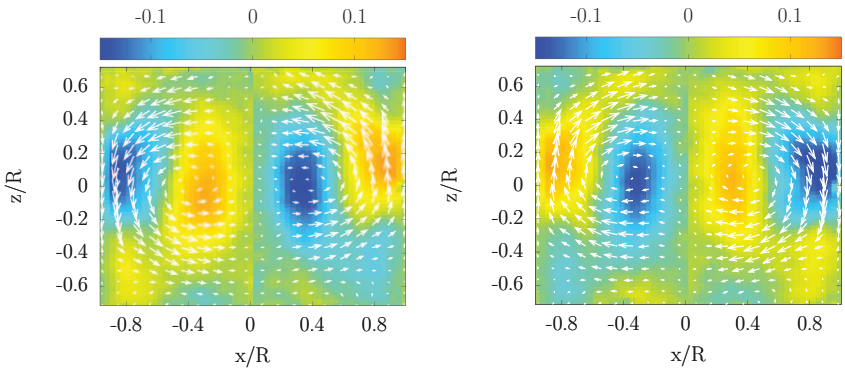

FIG. 9. Velocity fields obtained with the conditional average (left) $\mathbf{v}'(t[a_m(t) > \epsilon])$ in the plane $\varphi = [0; \pi]$ and (right) $\mathbf{v}'(t[a_m(t) < -\epsilon])$ in the orthogonal plane $\varphi = [\pi/2; 3\pi/2]$. Both are computed using the signal $a_m(t)$ and the horizontal lines represented in Fig. 8(a) for $\mathrm{Re} = 10^6$, $m = 3$, and $\epsilon = 0.2$. We clearly distinguish two pairs of azimuthal vortices, rotating around the azimuthal axis. The observed discontinuity at $x = 0$ is due to a slight shift of our S-PIV laser sheet from the center of the tank (enhanced online). [URL: http://dx.doi.org/10.1063/1.4855018.1]

in two planes, dephased by π. One indeed sees large scale structures looking like pairs of azimuthal vortices. By reproducing this conditional average using different phase φ_0 for B^{1mk_0} at a fixed m, we obtained the complete movie (see Fig. 9) of the rotation of this pair of vortices (see the Multimedia view). The physical mechanism leading to this vortices can be the Kelvin-Helmoltz instability laying in the shear layer, a secondary or related instability or the centrifugal instability. It is interesting to compare this result with the $m = 3$ velocity field shown in Fig. 2(d) using the same phase φ_0 as in Fig. 9(a). Both the anti-symmetric nature of the velocity field with respect to the $r = 0$ vertical axis and $\mathbf{v}(r = 0) = 0$ are recovered.

IV. SOME THEORETICAL CONSEQUENCES

In 1970, Kraichnan wrote a paper entitled "Instability in fully developed turbulence,"[28] in which he focuses on the propagation of errors from one range of scale to another. This problem is related to predictability of turbulence. In the present work, we consider another aspect of the same problem related to the stability of the unsteady coherent structures of a turbulent flow (in other words, to the dynamic of the perturbation of this given coherent structures). We have shown that using spatio-temporal spectra, and comparison or projection onto suitable Beltrami modes, it is possible to identify coherent perturbations to the time-averaged flow. This is liable to an Eckhaus instability analog to what is observed in systems in the laminar limit, with a few degrees of freedom. In classical phenomenology of turbulence the number of degrees of freedom scales like $\mathrm{Re}^{9/4}$. Given our range of Reynolds number (from 10^2 to 10^6), we thus can expect our system to be described by a number of degrees of freedom in the range 7×10^4 to 3×10^{13}. Our results thus prove that a huge number of degrees of freedom are irrelevant to describe the instability of our turbulent flow. This sets a number of interesting questions that we list below.

In the present paper, we have characterized experimentally the instability of the basic state. Is there any analytical or numerical way to explain our observations? Classical instability analysis for a given velocity field $\mathbf{v}(x, t)$ starts from stationary solutions of the Navier-Stokes equation:

$$\begin{aligned} \partial_j v_j &= 0, \\ \partial_t v_i + v_j \partial_j v_i &= -\frac{1}{\rho}\partial_i p + f_i + \nu \partial_k \partial_k v_i. \end{aligned} \tag{8}$$

In our case, we consider the instability of a time-average basic state $\bar{\mathbf{v}}(x, t)$ that obeys the equation:

$$\begin{aligned} \partial_j \bar{v}_j &= 0, \\ \partial_t \bar{v} + \bar{v_j} \partial_j \bar{v_i} &= -\frac{1}{\rho}\partial_i \bar{p} + \bar{f_i} + \nu \partial_k \partial_k \bar{v}_i + \partial_j R_{ij}, \end{aligned} \tag{9}$$

where $\rho\, R_{ij} = \rho\,(\bar{v}_i \bar{v}_j - \overline{v_i v_j})$ is the Reynolds stress tensor. This Reynolds stress represents the influence of all the degrees of freedom of the flow onto its average, and can, in general, only be computed via full solution of the NS equation. Therefore, the problem of instability of a mean turbulent flow cannot be tackled analytically or is too demanding numerically, unless a prescription (parametrization) of the Reynolds stress is provided. In the case of the plane Couette turbulent flow, for example, this was attempted by Tuckerman *et al.*[29] via the K-Ω closure model. They calculate steady 1D solution profiles of the K-Ω model and their linear stability to 3D perturbations, but find no correspondence between this analysis and the onset of turbulent-laminar bands in experiments and simulations. In the same way, Legras and Villone[30] address the problem of Kolmogorov flow instability when molecular viscosity is replaced by a Smagorinsky parametrization for small-scale turbulence. Such a parametrization represents the motion at scales smaller than the large scale Kolmogorov flow. They claim that it may provide hints on large-scale instabilities at large Re and, hopefully, on the character of such instabilities, but it has never been checked. In our case, it was observed that the sequence of Eckhaus instability resembles the sequence of instability observed at much lower Reynolds number.[12] This suggests that the replacement of the Reynolds stress by an eddy-viscosity might be a suitable parametrization by increasing the dissipation, and therefore decreasing

the effective Reynolds number (and the effective number of degrees of freedom). Theoretically, we note that the special geometry of our experiment and its parity symmetry properties make it plausible that the first term in the expansion of the Reynolds stress as a function of the velocity gradient is indeed quadratic, resulting in a non-isotropic eddy-viscosity tensor (in other words, there is probably no anisotropic kinetic alpha (AKA) term in the Reynolds stress expansion).[31] It is, however, not clear that the correct parameters of the instability (threshold, wavenumbers) can be captured with a simple eddy-viscosity model, since this procedure fails in the case of a plane Couette flow.[29] An interesting alternative would be to derive directly the mean state as the critical points of a suitable Arnold functional, making the problem liable to traditional tolls of bifurcation theory. Such strategy was followed in Ref. 32, resulting in a full description of a spontaneous parity-breaking turbulent bifurcation. The generalization of this model to non-axisymmetric mean state is however an open problem.

Summarizing, we have shown that the fluctuations of a turbulent von Kármán flow obey a sequence of Eckhaus-like instabilities with varying Reynolds number that is similar to the sequence of Eckhaus instability observed in the laminar flow, at much lower Reynolds number and that may be explained through a suitable parametrization by increasing the dissipation, and therefore decreasing the effective Reynolds number (and the effective number of degrees of freedom). If this is indeed true, it may have interesting implications for other fields, especially astrophysics and geophysics where Reynolds number are huge and our interest is mainly in the dynamics of the large-scale mean flow. For example, current climate models that have presently very low effective Reynolds number may be able to capture efficiently certain types of instabilities of the mean (climatic) turbulent state. They may, therefore, be more predictable that Kraichnan thought, in a very different meaning.

ACKNOWLEDGMENTS

E. Herbert acknowledges the support of the program DSM-Energie and is grateful to V. Padilla and C. Wiertel-Gasquet for techniques and B. Saint-Michel for interesting discussions.

[1] U. Frisch, *Turbulence: The Legacy of A.N. Kolmogorov* (Cambridge University Press, 1995).
[2] D. J. Tritton, *Physical Fluid Dynamics* (van Nostrand Reinhold Company, 1977).
[3] K. Sugiyama, R. Ni, R. J. A. M. Stevens, T. S. Chan, S.-Q. Zhou, H.-D. Xi, C. Sun, S. Grossmann, K.-Q. Xia, and D. Lohse, "Flow reversals in thermally driven turbulence," Phys. Rev. Lett. **105**, 034503 (2010).
[4] E. P. van der Poel, R. J. A. M. Stevens, K. Sugiyama, and D. Lohse, "Flow states in two-dimensional Rayleigh-Bénard convection as a function of aspect-ratio and Rayleigh number," Phys. Fluids **24**, 085104 (2012).
[5] B. Podvin and A. Sergent, "Proper orthogonal decomposition investigation of turbulent Rayleigh-Bénard convection in a rectangular cavity," Phys. Fluids **24**, 105106 (2012).
[6] P. K. Mishra, A. K. De, M. K. Verma, and V. Eswaran, "Dynamics of reorientations and reversals of large-scale flow in Rayleigh-Bénard convection," J. Fluid Mech. **668**, 480 (2011).
[7] M. Berhanu, R. Monchaux, S. Fauve, N. Mordant, F. Pétrélis, A. Chiffaudel, F. Daviaud, B. Dubrulle, L. Marié, L. Ravelet, M. Bourgoin, Ph. Odier, J.-F. Pinton, and R. Volk, "Magnetic field reversals in an experimental turbulent dynamo," Europhys. Lett. **77**, 59001 (2007).
[8] B. Gallet, J. Herault, C. Laroche, F. Pétrélis, and S. Fauve, "Reversals of a large scale field generated over a turbulent background," Geophys. Astrophys. Fluid Dyn. **106**(4–5), 468–492 (2012).
[9] G. K. Batchelor, "Note on a class of solutions of the Navier-Stokes equations representing steady rotationally-symmetric flow," Q. J. Mech. Appl. Math. **4**(1), 29–41 (1951).
[10] J. M. Lopez, J. E. Hart, F. Marques, S. Kittelman, and J. Shen, "Instability and mode interactions in a differentially driven rotating cylinder," J. Fluid Mech. **462**, 383–409 (2002).
[11] F. Moisy, O. Doare, T. Pasutto, O. Daube, and M. Rabaud, "Experimental and numerical study of the shear layer instability between two counter-rotating disks," J. Fluid Mech. **507**, 175–202 (2004).
[12] C. Nore, L. S. Tuckerman, O. Daube, and S. Xin, "The 1[ratio]2 mode interaction in exactly counter-rotating von Kármán swirling flow," J. Fluid Mech. **477**, 51–88 (2003).
[13] F. Ravelet, A. Chiffaudel, and F. Daviaud, "Supercritical transition to turbulence in an inertially driven von Kármán closed flow," J. Fluid Mech. **601**, 339–364 (2008).
[14] K. Stewartson, "On the flow between two rotating coaxial disks," Math. Proc. Cambridge Philos. Soc. **49**(02), 333–341 (1953).
[15] P. Zandbergen and D. Dijkstra, "Vonkarman swirling flows," Annu. Rev. Fluid Mech. **19**, 465–491 (1987).
[16] C. Nore, M. Tartar, O. Daube, and L. S. Tuckerman, "Survey of instability thresholds of flow between exactly counter-rotating disks," J. Fluid Mech. **511**, 45–65 (2004).
[17] P.-P. Cortet, E. Herbert, A. Chiffaudel, F. Daviaud, B. Dubrulle, and V. Padilla, "Susceptibility divergence, phase transition and multistability of a highly turbulent closed flow," J. Stat. Mech.: Theory Exp. **2011**, P07012.

[18] R. Monchaux, F. Ravelet, B. Dubrulle, A. Chiffaudel, and F. Daviaud, "Properties of steady states in turbulent axisymmetric flows," Phys. Rev. Lett. **96**(12), 124502 (2006).
[19] G. He, B. Dubrulle, and F. Graner, "Thermodynamical versus log-Poisson distribution in turbulence," Phys. Lett. A **245**, 419–424 (1998).
[20] P. Cobelli, P. Petitjeans, A. Maurel, V. Pagneux, and N. Mordant, "Space-time resolved wave turbulence in a vibrating plate," Phys. Rev. Lett. **103**(20), 204301 (2009).
[21] J. Boisson and B. Dubrulle, "Three-dimensional magnetic field reconstruction in the VKS experiment through Galerkin transforms," New J. Phys. **13**(2), 023037 (2011).
[22] P. Constantin and A. Majda, "The Beltrami spectrum for incompressible fluid flows," Commun. Math. Phys. **115**(3), 435 (1988).
[23] M. Rubio, P. Bigazzi, L. Albavetti, and S. Ciliberto, "Spatiotemporal regimes in Rayleigh-Benard convection in a small rectangular cell," J. Fluid Mech. **209**, 309–334 (1989).
[24] H. Chate and P. Manneville, "Transition to turbulence via spatiotemporal intermittency," Phys. Rev. Lett. **58**(2), 112–115 (1987).
[25] A. C. Newell and B. Rumpf, "Wave turbulence," Annu. Rev. Fluid Mech. **43**(1), 59–78 (2011).
[26] P. Coullet and G. Iooss, "Instabilities of one-dimensional cellular patterns," Phys. Rev. Lett. **64**(8), 866–869 (1990).
[27] P.-P. Cortet, P. Diribarne, R. Monchaux, A. Chiffaudel, F. Daviaud, and B. Dubrulle, "Normalized kinetic energy as a hydrodynamical global quantity for inhomogeneous anisotropic turbulence," Phys. Fluids **21**(2), 025104 (2009).
[28] R. H. Kraichnan, "Instability in fully developed turbulence," Phys. Fluids **13**(3), 569–575 (1970).
[29] L. S. Tuckerman, D. Barkley, and O. Dauchot, *Instability of Uniform Turbulent Plane Couette Flow: Spectra, Probability Distribution Functions and Kappa-Omega Closure Model* (Springer, New York, 2010), Vol. 18.
[30] B. Legras and B. Villone, "Stability of turbulent Kolmogorov flow," in *Progress in Turbulence*, Springer Proceedings in Physics Vol. 101, edited by P. D. J. Peinke, P. D. H. A. Kittel, D. S. Barth, and P. D.-I. M. Oberlack (Springer, Berlin, Heidelberg, 2005), pp. 99–102.
[31] B. Dubrulle and U. Frisch, "Eddy viscosity of parity-invariant flow," Phys. Rev. A **43**(10), 5355–5364 (1991).
[32] B. Saint-Michel, F. Daviaud, and B. Dubrulle, "A zero-mode mechanism for spontaneous symmetry breaking in a turbulent von Kármán flow," New J. Phys. (to be published).